Modeling topographic and climatic control of east-west asymmetry in Sierra Nevada glacier length during the Last Glacial Maximum

Mark A. Kessler,[1] Robert S. Anderson,[2] and Greg M. Stock[3]

[1]   Glaciers draining westward from the Sierra Nevada divide, California, during the Last Glacial Maximum (LGM) were ~7 times longer than east-draining glaciers. We address the degree to which this difference may be attributed to the topographic asymmetry of the west-tilted Sierran block and the climate asymmetry resulting from orographic modification of Pacific Ocean storms. We simulate kilometer-scale glaciers within the 50 × 50 km Kings Canyon region of the southern Sierra by employing a two-dimensional numerical model that is driven by simple, spatially variable climates and treats ice transport by deformation, sliding, and avalanching. In numerical experiments, we match simulated termini to LGM moraine positions to constrain the parameters of different climate scenarios. The 38-km-long LGM glacier in Kings Canyon was reproduced by a climate specified by an equilibrium line altitude (ELA) of 3170 m, a mass balance gradient of 0.01 m/yr/m, and a maximum positive balance of 2 m/yr. This climate generates much shorter (average ~6 km long) east-draining glaciers that, however, overshoot the LGM moraines by ~1 km. Roughly 97% of the E-W difference in glacier lengths can therefore be attributed to topographic asymmetry alone. A second experiment suggesting a 120-m-higher ELA of 3290 m east of the divide can explain the shorter east-draining glaciers. An experiment in which orographic precipitation is explicitly simulated and melt is prescribed using a positive degree-day algorithm matches both Kings Canyon and the average east-draining glacier length with an LGM climate that was 5.6°C cooler and ~2 times wetter than the modern Sierra Nevada.

1.   Introduction

[2]   Former glaciations of the Sierra Nevada of California displayed a strong asymmetry in glacier lengths between the western and eastern flanks of the range [e.g., *Birman*, 1964; *Wahrhaftig and Birman*, 1965; *Moore*, 2000]. Glacial extents delineated by moraines and trimlines indicate that Pleistocene glaciers on the eastern flank were less than 20 km in length while those on the western flank were as long as 100 km [*Wahrhaftig and Birman*, 1965, and references therein]. During the Last Glacial Maximum (LGM), known locally as the Tioga Glaciation [*Blackwelder*, 1931; *Clark et al.*, 2003], the main trunk glacier occupying Kings Canyon on the western flank was ~38 km long (Figure 1), roughly 7 times the length of the average glacier on the opposing eastern flank [*Moore*, 2000]. This skewed pattern of glacier

lengths has been attributed to strong asymmetries in topography and climate. The western flank of the Sierra Nevada has a much lower slope and consequently longer valleys than the eastern flank (Figure 1) [e.g., *Bateman and Wahrhaftig*, 1966]. During the LGM, these lower-sloped valleys would have had much larger snow accumulation areas; assuming a uniform equilibrium line altitude (ELA, the altitude of the line in the landscape separating net accumulation of ice above and net ablation of ice below) of ~3100 m (determined for the eastern flank [*Gillespie*, 1991; *Clark et al.*, 2003]), the western flank had four times the accumulation area of the eastern flank (Figure 2). In addition to this distinct topographic asymmetry, the Sierra Nevada also displays a remarkable asymmetry in climate (Figure 3). The modern Sierra Nevada receives most of its wintertime precipitation from storms impinging from the southwest, which is an ideal direction for generating strong orographic influence on precipitation over this southeast-to-northwest trending range [e.g., *Pandey et al.*, 1999]. Uplift and cooling of air masses as southwesterly storms cross the range produce heavy precipitation on the western flank. As these water-depleted air masses pass over the crest, they descend to warmer elevations and expand, inhibiting further precipitation and casting a substantial rain shadow into the western Great Basin. For example, the Fresno Airport

---

[1]Institute for Arctic and Alpine Research, University of Colorado, Boulder, Colorado, USA.
[2]Department of Geological Sciences and Institute for Arctic and Alpine Research, University of Colorado, Boulder, Colorado, USA.
[3]Department of Geological Sciences, University of Michigan, Ann Arbor, Michigan, USA.
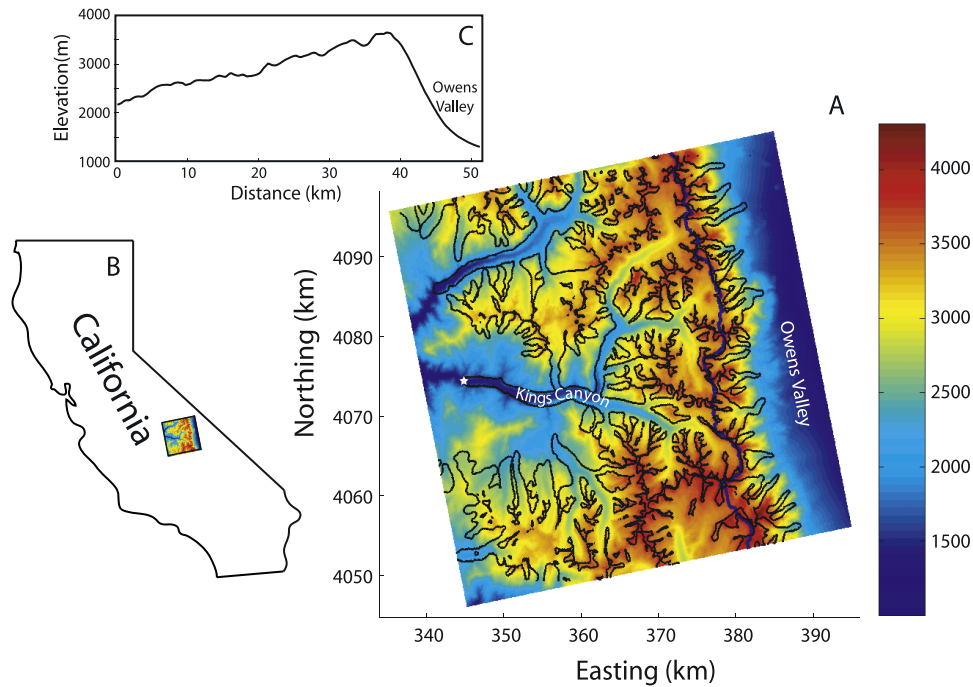
Figure 1. Location and topography of the study area. (a) False color image of the southern Sierra Nevada, California, in the vicinity of Kings Canyon, with (b) location within California. Range crest (blue line) averages ~3900 m. Extent of Last Glacial Maximum (LGM) glaciation (Tioga glaciation) is shown by black line [*Moore*, 2000]. LGM glacier terminus location in Kings Canyon (star) is at ~1300 m. (c) Swath-averaged topographic profile perpendicular to range crest; a distinct topographic asymmetry.

station on the western, upwind side of the range receives twice as much precipitation (28 cm/yr) as the Independence station on the eastern, lee side of the range (13 cm/yr) despite the Independence station being 1100 m higher in elevation (Western Regional Climate Center, Climate summaries of Southern California meteorological stations, 2004, http://www.wrcc.dri.edu/summary/climsmsca.html) (hereinafter referred to as WRCC, http://www.wrcc.dri.edu/summary/climsmsca.html).

[3] The effects of topographic and climatic asymmetry on glacier length in the Sierra Nevada have been considered before [e.g., *Wahrhaftig and Birman*, 1965]; however, there
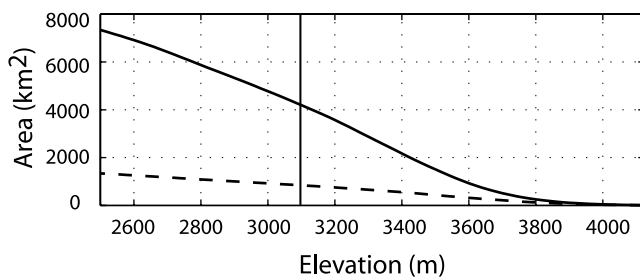
has been no quantitative assessment of their respective effects. We use numerical simulations of glaciers, in which we can turn on and off various processes, to assess the independent contributions of topography and climate on the length of LGM glaciers in Kings Canyon and the opposing
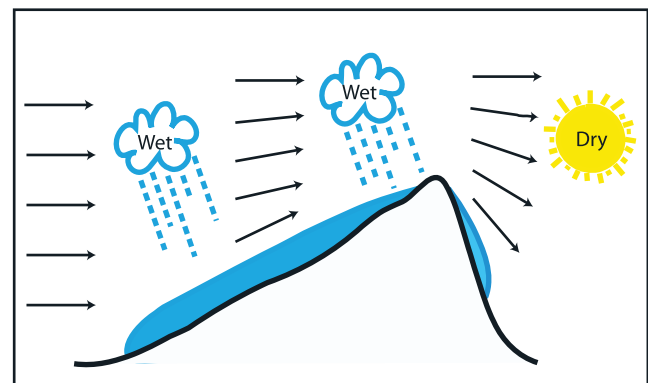

Figure 2. East-west Sierra Nevada hypsometry. Area above a given elevation for the 50-km-long section of the Sierra Nevada range centered about Kings Canyon shown in Figure 1. Solid line is the western flank, dashed line is the eastern flank. Given an LGM ELA of 3100 m, the western flank would have had 4 times the accumulation area as the eastern flank.

Figure 3. Schematic diagram of a profile of the Sierra Nevada showing two hypothesized reasons for longer and lower elevation glaciers forming on the western flank: (1) Lower average slope on the western flank results in a much larger accumulation areas (see also Figure 2) and (2) uplift, convergence, and cooling of air masses predominantly from the southwest results in strong precipitation on the western flank, while lowering, expansion, and warming cause a precipitation shadow on the eastern flank.

eastern flank, and compare our results to observed LGM termini positions and inferred ELAs.

[4] We view the simulations presented here as one step toward the goal of basing the reconstruction of paleoclimate from glacial geologic information entirely on the physics of glaciers, climate, and topography. Although simple methods exist to assess past ELAs from moraine positions, these should be reevaluated in light of modern understanding of both the climatic forcing and the glaciological response to it. We ultimately hope to incorporate these numerical simulations of alpine glaciers into models of long timescale landscape evolution, and long timescale variation in sediment discharge to the fluvial and depositional systems downstream. We must first, however, demonstrate that this glacial model can match the most robust physical constraints available, data sets of LGM glacier positions.

[5] Geomorphic observations, including moraine positions and trimlines from paleo-glaciers, have been used by many authors to infer paleoclimate properties. Most commonly, these constraints are used to determine the former ELA by assuming a specific ratio of accumulation area to total glacier area (AAR) [e.g., *Meierding*, 1982; *Porter*, 1975; *Gillespie*, 1991; *Burbank*, 1991]. Using just the glacier footprint, and assuming an AAR typical of temperate valley glaciers of 0.65 [*Meier and Post*, 1962; *Meierding*, 1982], one can estimate the paleo-ELA, and thereby infer a paleoclimate. This method is widely used because it is a straightforward calculation and the observational data with which to implement it are often preserved in the geomorphology. However, this simple method has potential for large errors that limit its accuracy for paleoclimate reconstructions because it assumes a constant AAR. Actual measured AARs typically lie between 0.5 and 0.8 [*Meier and Post*, 1962]. In addition, an accurate calculation of the AAR requires that the ELA be considered at the ice surface, which can be well above the observable valley floor. The horizontal position of the ELA shifts downvalley as the glacier thickens, effectively capturing more accumulation area, which therefore acts as a positive feedback on glacial extent.

[6] Finally, one might wish to constrain properties of a past climate besides the ELA (e.g., temperature, wind velocity, precipitation rate). Reconstructions of climate can be accomplished by dividing the change in ELA from the LGM to the present by a lapse rate to estimate the required temperature depression in the LGM [e.g., *Smith et al.*, 2005]. Separating the change in net mass balance estimated from ELA reconstructions into precipitation and melt components would further constrain climate forcing of glaciers.

[7] The method used here to estimate paleo-ELAs and climates is to simulate numerically many glaciers within a mountainous topography for a variety of imposed climates, evaluating each simulation by the degree to which it reproduces the observed moraine patterns. A similar technique has been applied by *Plummer and Phillips* [2003] to the Bishop Creek basin in California. The numerical model used here allows us to specify climates of any degree of complexity, from simple three-parameter climates to complex climates in which patterns of precipitation and melt are explicitly calculated. By including climate and ice dynamics in a single model, we are able to capture feedbacks between glaciers and climate; for example, the increase in accumu-

lation area as glaciers thicken is explicitly captured. The effects of the topography are therefore captured more completely than when employing a simple map-view AAR calculation. In addition, performing these calculations across a wide area that includes many glacial valleys yields a more robust prediction of the paleoclimate. The details of climate and topography in any one valley do not strongly steer our assessment.

2. Numerical Model

[8] We developed a two-dimensional finite difference numerical model that simulates the formation and evolution of temperate valley glaciers on a two-dimensional topographic surface with a specified meteorological setting. Driven by a time series of mass balance (snow precipitation - melt rate), the model calculates ice surface elevations above a two-dimensional terrain by solving equations for ice flux and mass conservation using explicit methods. A number of other authors have employed one- and two-dimensional models based on similar sets of equations [e.g., *Oerlemans*, 1986; *MacGregor et al.*, 2000; *Plummer and Phillips*, 2003]. However, the model developed for this study integrates glacier and climate simulation components explicitly, and thus has the unique ability to simulate feedbacks between the changing ice surface and the climate forcing. In addition, the framework of this model permits the inclusion of discrete processes that modify the ice distribution, such as avalanching on steep terrain. The efficiency of this model allows us to simulate glacial evolution over millennial timescales at spatial scales that resolve valley glaciers. Finally, from a computational standpoint, the simplicity of this model permits the investigation of significant regions of parameter space, allowing us to determine the effect of new processes or altered algorithms for them.

2.1. Conservation of Mass

[9] The core of this numerical model is conservation of mass at each cell in a regular two-dimensional grid (Figure 4). Change in ice thickness at each grid cell is calculated using the continuity equation,

$$\frac{dh_i}{dt} = b_z - \frac{dq_x}{dx} - \frac{dq_y}{dy},\qquad(1)$$

in which h_i is the ice thickness at a node in a two-dimensional lattice, and b_z is the rate of accumulation or ablation of ice (we assume a uniform ice density of 917 kg/m^3, including freshly precipitated ice). Here q is the volumetric specific discharge [L^3/LT] of ice into and out of a cell from neighboring cells,

$$q = h_i(U_d + U_s),\qquad(2)$$

in which U_d is the depth-averaged velocity of ice owing to ice deformation, and U_s is the sliding velocity. We discuss the calculation of b_z, U_d and U_s below.

[10] The primary obstacle in constructing this numerical model is that the entire simulation space is not covered with ice; therefore internal boundaries between rock and ice exist, and special measures must be taken to ensure ice is
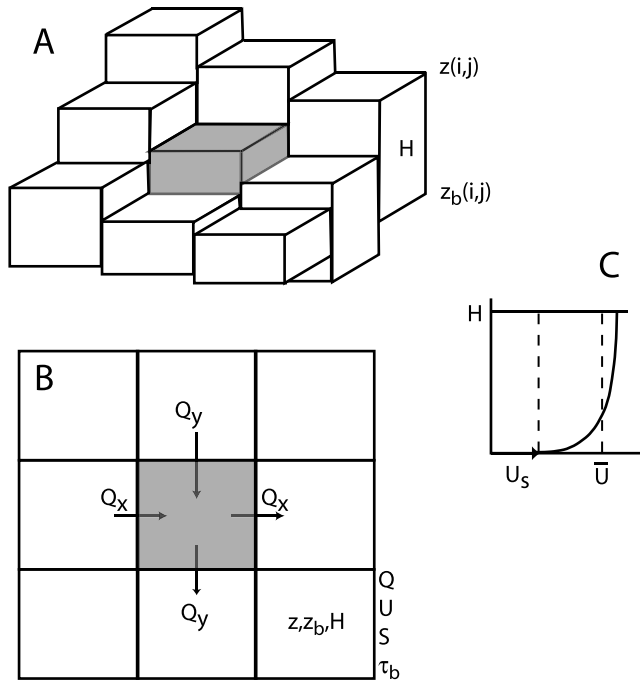
Figure 4. Schematic of the model setup. (a) Nine cells of the calculation space, with 200×200 m spacing. Ice thickness, H, is difference between ice surface elevation z and bedrock elevation, z_b. (b) View from top showing ice discharges, Q, to and from the central cell. Bottom right cell shows those variables calculated within a cell, and those calculated across cell boundaries (S = ice surface slope, τ_b = gravitational driving stress). (c) Ice speed profile showing sliding speed, U_s, and deformation rate profile. Ice discharge Q is calculated from $Q = H\bar{U}$.

not created or lost at those boundaries. Our model conserves ice to within 0.01% over the duration of the simulations presented here, the longest of which are ~10,000 years and roughly a million time steps. For an in-depth discussion of the challenges of constructing a similar two-dimensional finite difference model for glaciers we refer the reader to *Plummer and Phillips* [2003].

2.2. Mass Balance

[11] The local climate of a temperate alpine glacier can be defined by the net mass balance, which is the sum of the accumulation by snow precipitation and the loss by ablation. We have employed several schemes to prescribe the mass balance.

2.2.1. Net Mass Balance

[12] In our initial simulations, we prescribe a simple mass balance that combines accumulation and ablation into a single thresholded linear mass balance function of elevation (Figure 5),

$$b_z = \min\{\nabla b_z(Z_i - ELA), b_z^{max}\}, \qquad (3)$$

in which ∇b_z is the gradient in mass balance with elevation, Z_i is the ice surface elevation, *ELA* is the elevation of zero net mass balance, and b_z^{max} is a prescribed maximum mass balance that accounts for the depletion of moisture available

for precipitation at higher elevations. We chose this three-parameter mass balance function to reproduce the gross characteristics of measured mass balance functions on modern glaciers in western North America [*Meier et al.*, 1971; *Mayo*, 1984], and specifically those of the orographically influenced mass balance across the Sierra Nevada. The observation that the mass balance gradient generally declines and flattens out in the accumulation zone [e.g., *Meier and Post*, 1962] is included by limiting the mass balance to a maximum of b_z^{max}. The variation in glacier extent with ELA was explored; however, in the simulations shown here, we used values for the mass balance gradient ($\nabla b_z = 10$ m/yr/km) and maximum mass balance ($b_z^{max} = 2$ m/yr) [*Meier et al.*, 1971; *Mayo*, 1984] that are typical for glaciers in western North America.

2.2.2. Orographic Precipitation and Positive Degree-Day Melt

[13] In additional simulations, we incorporate an orographic precipitation model [*Roe et al.*, 2002] into this glacial model to calculate explicitly the effect of topography on the spatial variation in precipitation from an air mass forced over the range. Because the primary source of winter precipitation is from storms coming from the southwest [e.g., *Pandey et al.*, 1999], orographic modification of the precipitation pattern is important. A melt model based upon a positive degree-day algorithm was used to determine the ablation of ice. The sum of the solid phase precipitation and the melt yields the net mass balance.

[14] As summarized by *Roe et al.* [2002], an air mass moving across a mountain range is forced to ascend to higher and cooler elevations, causing the air column to saturate and excess moisture to precipitate (Figure 3). The convergence of the column moisture flux can be expressed as

$$-\nabla \cdot \vec{F} = \left(\alpha_0 + \alpha_1 \bar{v} \frac{dz}{dx}\right) e_{sat}(T_s), \qquad (4)$$

in which α_0 ($= P_0/e_{sat}(T_0)$) scales ∇F to match the prescribed far field precipitation (P_0) where $dz/dx = 0$, and T_0 is the far field surface temperature; α_1 ($= C_\alpha e_{sat}(T_0)$) scales the topographically derived precipitation, in which C_α is fitted to simulate modern precipitation patterns for modern temperatures; $\bar{v}$ is the wind velocity; and $e_{sat}(T_s)$ is the saturation vapor pressure, given by $e_{sat}(T_s) = 6.112 e^{17.67 T_s/(243.5 + T_s)}$, where T_s is the local surface temperature [*Roe*, 2005].
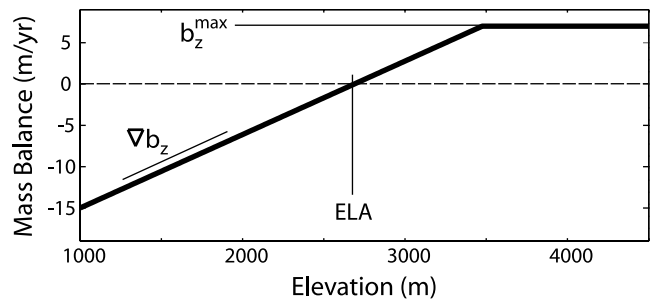

Figure 5. Example net mass balance function (bold line) described by three parameters: the maximum mass balance (b_z^{max}), the mass balance gradient (∇b_z), and the equilibrium line altitude (ELA).
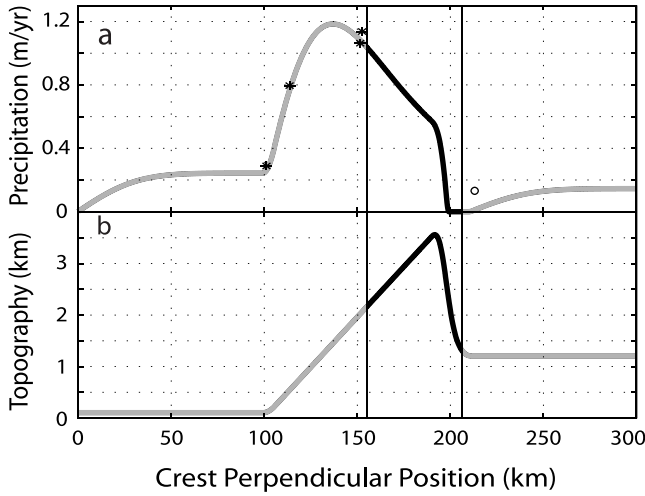
Figure 6. (a) Orographically derived precipitation over (b) a typical Sierra Nevada profile encountered by winds from the southwest. The zone of bold black lines denotes the area of the glacial simulation. Asterisks denote meteorological recording stations used to calibrate the orographic model; from left to right, they are Fresno Airport, Balch Power House, Grant Grove, and Lodgepole; the circle off the eastern flank indicates the meteorological recording station at Independence (WRCC, http://www.wrcc.dri.edu/summary/climsmsca.html). These sites are plotted at the horizontal position for which the elevation in Figure 6b is equal to the station elevation.

[15] Saturation does not translate to precipitated hydrometeors on the ground directly below. Instead, the hydrometeors impact downwind; the precipitation rate at any location will therefore integrate the upwind moisture flux over some smoothing length scale (Δx) [*Roe et al.*, 2002; *Alpert*, 1986],

$$\dot{p}(x) = S \frac{\Delta x \pi}{2} \int_x^\infty -\nabla \cdot \vec{F} \times e^{-[(x-x')/\nabla x]^2} dx'. \qquad (5)$$

Here S is a scaling factor that ensures precipitation is conserved. We have adjusted C_α and Δx such that the orographic model reproduces modern patterns of precipitation across the Sierra Nevada when forced with modern temperature records and an average storm wind velocity of 10 m/s (Figure 6). The value of Δx can be considered the wind velocity multiplied by the time it takes for an average hydrometeor to impact the ground. The fitted value of Δx (35 km) coincides with an average fall distance of 3.5 km (the moisture scale height [*Roe*, 2005]) and a settling velocity of 1 m/s (which is reasonable for snow [*Roe*, 2005]).

[16] In our model, only precipitation falling in a solid form contributes to the mass balance of the glacier. The phase of the precipitation is calculated using the ground surface temperature, T_s, which both declines linearly with surface elevation and varies sinusoidally in time,

$$T_s(z,t) = T_s(z_o,t_o) + A_T \sin(2\pi(t-t_o)/\tau) + \Gamma(z-z_o), \qquad (6)$$

in which Γ is the atmospheric lapse rate (-6.5 °C/km [*Roe*, 2005]), τ is the period of oscillation (i.e., $\tau = 1$ year), and

A_T is the half-amplitude of the temperature swing. Seasonal variations prescribed by equation (6) are accounted for in calculating both the solid phase precipitation and the melt; from these the net annual mass balance (b_z) is calculated for use in equation (1).

[17] The surface temperature history is used to calculate the history of melt rate (m/yr) at each cell using a positive degree-day method [e.g., *Braithwaite*, 1995],

$$\dot{m} = kN_{pdd}\overline{T}_{pdd}, \qquad (7)$$

in which k is the positive degree-day factor ($k = 0.008$ m/d/ °C [*Braithwaite*, 1995]), N_{pdd} is the number of days per year with a mean temperature above 0°C, and $\overline{T}_{pdd}$ is the mean temperature for those days.

[18] In the simulations shown here the orographic precipitation is calculated over a one-dimensional simplified topography perpendicular to the prevailing wind direction (Figure 6b). This simplified topography has a linear ramp on the western flank, with slope equal to the swath-averaged Sierra topography, and a smoothed version of the swath-averaged topography on the eastern flank. Collapsing the topography in this manner simplifies the precipitation pattern and acknowledges that air masses respond to topography on scales much larger than the 200 m cells in this model. This approach neglects the effect of valley-scale topographic steering on precipitation [*Anders et al.*, 2004]. In contrast, the melt model, which depends on local conditions (i.e., temperature), is applied with elevations given by the full two-dimensional topography.

2.3. Ice Flux

[19] In this model, ice is transported between cells via two continuum processes, ice deformation and basal sliding, and one discrete process, avalanching. In each case we seek the specific volumetric discharge of ice, or volume per unit width per unit time.

2.3.1. Ice Deformation

[20] Deformation of ice within a glacier acts to transport ice in the direction of the local ice surface slope. We employ the shallow ice approximation [e.g., *Paterson*, 1994], in which ice discharge is driven only by the stress associated with the local ice surface slope. The depth-averaged velocity due to ice deformation is given by

$$\overline{U}_d = \frac{2}{5}Ah_i\tau_b^n, \qquad (8)$$

in which A is the coefficient of Glenn's flow law, h_i is the ice thickness, and τ_b is the gravitational driving stress: ($\tau_b = \rho g h_i \nabla Z_i$, in which Z_i is the ice surface elevation). In reality, A is a function of many factors, including, but not limited to, water content, temperature, pressure, and included particulate matter; we use the recommended value of 6.8×10^{-15} s^{-1} (kPa)$^{-3}$ for temperate glaciers [*Paterson*, 1994], and ignore temperature effects because the alpine glaciers we seek to simulate are temperate. The flow law exponent n is generally taken to be 3 for glacier ice under normal environmental conditions [e.g., *Paterson*, 1994]; this value is used here.

2.3.2. Ice Sliding

[21] The processes that contribute to basal sliding are less well understood than those controlling ice deformation.
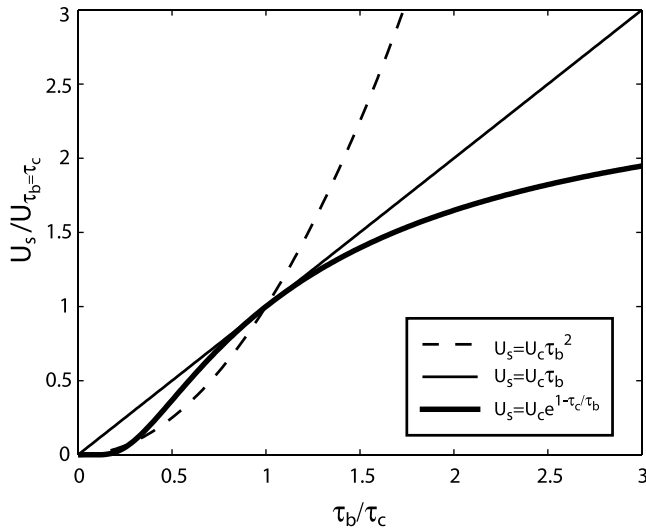
Figure 7. Normalized sliding laws showing relationship between sliding rate and gravitational driving stress. Sliding velocities are scaled by their value at the critical driving stress, τ_c. Dashed line is the standard second power formulation [e.g., *Paterson*, 1994; *Plummer and Phillips*, 2003], thin solid line is the formulation of *Marshall et al.* [2005] with dependence on hydrologic variables removed, and solid bold line is the function used here. As with the standard formulation, the formulation used here approaches zero at $\tau_b = 0$; unlike other formulations, the velocity used here is limited at high gravitational driving stress.

These include regulation and block sliding, as well as localized deformation near the bed. The presence of a thin layer of water separating the ice from the bed simplifies the problem by allowing a zero shear stress approximation; however, friction between the bed and rocks embedded in the ice is no less difficult of a problem, given that it depends on the spatial distribution of rock concentration as well as the physics of viscous flow around individual rocks that can potentially stick and slip with respect to the bed. Also, sliding velocity (U_s) is difficult to quantify because on short timescales it is a strong function of the often-unknown glacial/subglacial hydrology [e.g., *Iken and Bindschadler*, 1986; *Anderson et al.*, 2004], although progress is being made in modeling glacier hydrology [*Flowers and Clarke*, 2002a, 2002b; *Marshall et al.*, 2005].

[22] We have made no attempt in the numerical modeling reported here to capture the glacial hydrology or sliding physics at small length scales or short timescales; treating the spatial and temporal variability of glacial/subglacial hydrology and its interactions with ice motion, which occur on timescales from diurnal to decadal, would greatly complicate the simple model of glaciers presented here. Although it is possible to incorporate a glacial hydrological model with a model for ice motion [e.g., *Kessler and Anderson*, 2004; *Marshall et al.*, 2005], this is computationally expensive and the timescales of the hydrological system are short compared to the timescales of interest in this study.

[23] We have chosen a simple formulation of the sliding velocity that meets three criteria: (1) the sliding velocity is very small at low gravitational driving stress ($\ll$ 1 bar) and zero when the gravitational driving stress is zero; (2) the

sliding velocity increases rapidly within some range of gravitational driving stresses; and (3) the sliding velocity remains finite at high gravitational driving stresses ($\gg$ 1 bar). Although this formulation does not include explicitly the glacial hydrology, these three properties should remain unchanged with its inclusion. An ideal formulation for sliding velocity might calculate sliding from first principles and measurable quantities without unconstrained coefficients. However, as the inner workings of the sliding mechanism are not well known, we have chosen to use a simple formulation in which the parameters are measurable and for which substantial intuition exists. Many formulations for basal sliding have been developed for numerical modeling of glacier motion; an overview of several simple sliding formulations is given in Appendix A.

[24] In temperate alpine glaciers, it is commonly observed that the gravitational driving stress is within a narrow range of values around 1 bar (or 10^5 Pa) [e.g., *Paterson*, 1994; *Hooke*, 2005]. We interpret the narrow observed range of τ_b values as indicative of an attractor state toward which glacier systems tend from a wide range of initial conditions, and basal sliding as a mechanism that brings the gravitational driving stress toward that state. Large values of τ_b produce significant sliding, transporting ice efficiently between adjacent locations, thus reducing the local surface slope and, thereby, the gravitational driving stress. We express the sliding velocity as

$$U_s = U_c e^{1-\frac{\tau_c}{\tau_b}}, \tag{9}$$

in which U_c is a typical sliding velocity and τ_c is the gravitational driving stress that gives rise to this typical sliding velocity. The values of $U_c = 20$ m/year and $\tau_c = 1$ bar $= 10^5$ Pa were used in the simulations shown here. In practice, the model is relatively insensitive to the sliding law parameter values; more conservative estimates of sliding (i.e., lower U_c or higher τ_c) result in higher average ice thickness and gravitational driving stress that then result in greater motion by ice deformation. This formulation of the sliding velocity maintains sliding within reasonable bounds between 0 (when $\tau_b \ll \tau_c$) and eU_c (when $\tau_b \gg \tau_c$) (Figure 7). We note that the sliding is less sensitive to τ_b at high gravitational driving stresses than in a τ_b^2 sliding law; this is advantageous in that the relatively poorly constrained process of sliding is conservatively estimated. We also acknowledge that this formulation neglects some relevant physics (e.g., subglacial hydrology and till deformation), which can cause behaviors quite different from those proposed here, such as rapid sliding at low gravitational driving stresses. However, as the general trend in sliding with the gravitational driving stress remains positive for all cases, these behaviors could be crudely modeled through the parameter τ_c.

2.3.3. Snow Avalanching

[25] High, steep terrain in glaciated mountain ranges typically remains free of snow even when lower altitudes host substantial glaciers. This condition results from topographic controls of both depositional processes (e.g., strong winds preventing deposition), and post-depositional processes (e.g., snow avalanching on steep slopes).

[26] In this model, we employ post-depositional avalanching as a discrete process that transports ice away from

steep surfaces. After the ice surface heights have been updated for ice continuity during that time step (equation (1)), we employ an avalanching routine similar to routines used for sand avalanching [e.g., *Bak et al.*, 1988; *Werner*, 1995]. From all cells that exceed a prescribed slope a small volume of snow is moved downslope. This process is repeated until the gradient is everywhere below a prescribed maximum slope (=30°), or until bedrock is exposed. A similar approach of moving parcels of snow between cells has been employed to model glacier dynamics by using the gravitational driving stress of 1 bar as the criterion for stability [*Harper and Humphrey*, 2003]. Since the time step required for numerical stability of equation 1 is quite small (∼1 day), and the avalanching algorithm is computationally expensive, the avalanching routine is not run every time step. Instead, avalanching occurs at random intervals with a frequency of several events per year; more frequent avalanching has no noticeable effect on model results.

3. Four Numerical Experiments

[27] We report results from four numerical experiments. The first three experiments test the sensitivity of the asymmetry in glacial extents between Kings Canyon and the opposing eastern flank to various climate scenarios. In the first experiment we use the simplest climate formulation to calculate the best-fitting LGM ELA on the western flank and isolate the contribution of topography to the east-west asymmetry in glacier lengths. In the second experiment we determine the change in ELA on the eastern flank needed to explain the residual east-west asymmetry in glacier lengths after topography has been accounted for. In the third experiment we use the explicit orographic model for precipitation and the positive degree-day method for melt to explore what temperature and precipitation anomaly combination produces an east-west asymmetry in climate sufficient to explain the residual asymmetry in glacial extent. In a fourth and final experiment we determine the north-south gradient in temperature that best simulates the observed north-to-south rise in termini elevations and ELA. In all of these experiments, we compare quantitatively the simulated glacial extents with mapped LGM glacier termini positions in Kings Canyon and on the opposing eastern flank [*Moore*, 2000].

[28] The topography used in these simulations is derived from 10 m USGS DEMs of the Kings Canyon area, decimated to a 200-m grid spacing (Figure 1). The boundaries of the simulation space were chosen to go well beyond the drainage divides of the valleys of interest, and were prescribed to be ice-free at all times.

3.1. Experiment 1: Western Flank Equilibrium Line Altitude Lowering

[29] In the first numerical experiment, we used a three-parameter climate (equation (3) and Figure 5) to determine the ELA that best replicates the extent of glaciation in Kings Canyon during the LGM. We initiated the simulation with the ELA set near the maximum bedrock surface elevation in the simulated space. The ELA was then lowered in increments of 50 m at 400-year intervals to allow the glacier to approach a new steady state configuration. As the simulated glacier terminus neared the LGM terminus position in Kings

Canyon, the ELA was lowered in 10-m intervals in another simulation.

[30] During this ELA-lowering experiment the glacier margins monotonically descended down Kings Canyon and neighboring valleys (Figure 8; 2-D and 3-D movies of this ELA-lowering experiment are provided in the auxiliary material[1]). As glaciers enlarged during steady-ELA intervals, ice thickening increased surface elevations, thereby increasing the accumulation area of each glacier. Correctly accounting for this change in surface height with ice thickening is one challenge of methods of determining paleoclimate that rely upon the accumulation area ratio. The maximum error in accumulation and ablation areas, which would only be made by an overly simplistic calculation of the AAR that neglected ice thickness entirely, is given by the difference between the green and black lines in Figure 8c. While the actual AAR based upon an ELA at the ice surface is 0.68, the AAR calculated using the bedrock surface is 0.59.

[31] The intrinsic, or e-folding, timescale (τ, the time it takes for the distance from steady state to decrease by a factor of 1/e) of the glacier footprint area determines the ability of this lowering schedule to reach steady state between lowering events. Prior to running this experiment, we determined an approximate value for τ by fitting an exponential function $A^{fp} - A_0^{fp} = c_{dA} \left(1 - e^{-(t - t_0)/\tau}\right)$ to the glacier footprint area (A_{fp}) following an instantaneous lowering of the ELA at $t = t_0$ (Figure 9). Here c_{dA} is the long timescale change in footprint area. However, the response time of a glacier to climate change is a function of its size, as well as the climate and the topography over which it passes. This is reflected in the change in intrinsic timescale as the glacier grows (Figure 9). Initially, the characteristic timescale is only a decade or two, but as the glacier enlarges the timescale increases. After an initial increase in timescale to approximately 50 years, the timescale fluctuates about that value, likely reflecting peculiarities of the terrain. The imposed 400-year (8τ) schedule of ELA lowering should allow the glacier footprint area to have achieved 99.97% of its steady state area before the next ELA lowering event; hence we are assured that the terminus reaches the steady state position associated with each ELA.

[32] For each imposed ELA, the terminus was located by identifying the lowest cell within Kings Canyon containing ice greater than 1 m thick (Figure 10a). The minimum distance from this cell to the observed LGM terminus position (star in Figure 1) was then determined to assess the goodness of fit of the simulated glacier, with its corresponding ELA, to the LGM Kings Canyon glacier (Figure 10b). Below 3200 m the ELA was lowered in 10 m increments; the best-fitting ELA was 3170 m.

[33] This methodology for determining the paleo-ELA compares the observed moraine positions with an ice margin that reflects a climate that is steady over several hundred years. By allowing the simulated glaciers to reach the maximum possible ice extent for the imposed climate, this methodology likely causes an underestimation of the severity of the climate that produced the observed moraines.
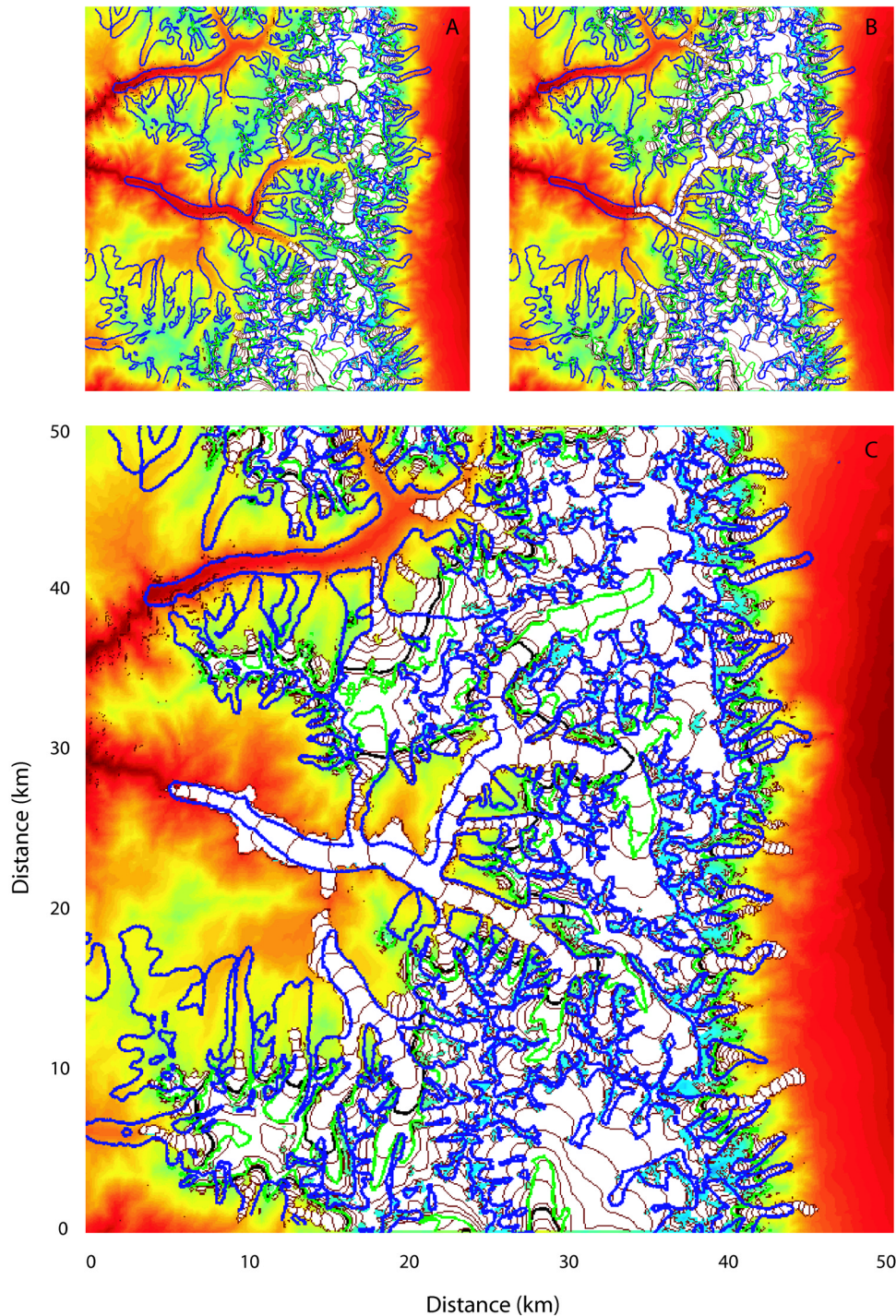
Figure 8. Steady state glacier extents for three ELA values: (a) 3500 m, (b) 3350 m, and (c) 3170 m. Blue line indicates measured LGM glacial extents extracted from *Moore* [2000]; black line indicates the ELA at the ice surface; green line indicates the ELA at the bedrock surface. Simulation space does not encompass the full drainage areas of canyons to the north of South Fork Kings Canyon, resulting in large misfits.

[34] Inspection of the eastern and western glacial footprints with an imposed uniform ELA of 3170 m reveals that much of the strong asymmetry in glacial lengths is due to the topography. Taking the longest straight-line distance from the terminus to the farthest reaches of the accumulation zone as the glacier length, at an ELA of 3170 m, the Kings Canyon glacier is 37.8 km long. In contrast, the

average simulated eastern flank glacier length is 5.9 ± 2.1 km (mean ± std. dev.). By comparison, the mean observed LGM eastern flank glacier length extracted from *Moore's* [2000] map of LGM glacial extents is 5.1 ± 2.0 km; the real glaciers were shorter than those we have simulated with a uniform climate. Roughly 97% of the 32.7 km difference in glacier lengths between eastern and western
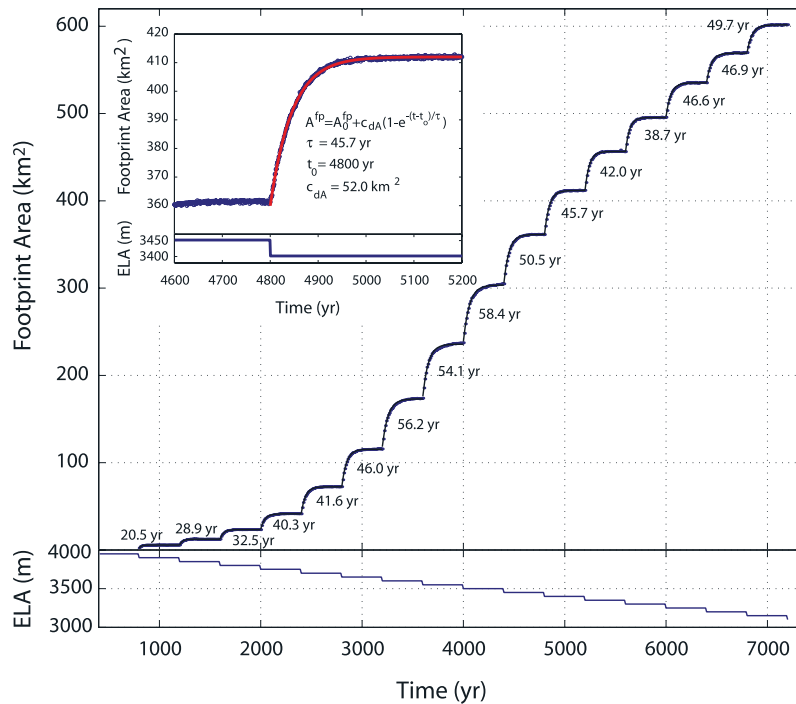
Figure 9. Kings Canyon glacier footprint area (dots) in a simulation in which the ELA (blue line) was decreased in 50-m steps at 400-year intervals. The intrinsic timescale of the glacier dynamics is given (in years) for each ELA interval, calculated assuming an exponential approach to steady state (red lines). Inset shows evolution of the glacier footprint area after one 50-m-step lowering of the imposed ELA. The intrinsic timescale for each interval is found by fitting the equation shown (bold red curve).

flanks, or 85% of the ratio of glacier lengths, can be attributed to topographic asymmetry, with no asymmetry in climate. However, most of the simulated eastern flank glaciers overshoot their measured positions: 80% of the simulated glaciers exceed their LGM termini positions by an average of 1210 m.

[35] In this numerical model, ice motion due to sliding is expressed by equation (9), which sets a typical and maximum sliding velocity by introducing two parameters, the characteristic gravitational driving stress (τ_c) and the characteristic sliding velocity (U_c). Factor of 2 changes in either of these parameters produced only 10- to 20-m changes in the predicted LGM ELA. Despite the poor constraint on the magnitude and physics of sliding, that the predicted ELA is insensitive to the sliding parameters is encouraging for the use of this technique in predicting paleoclimate. In arriving at our final formulation of the sliding rule, we tested many variants. In general, the effects on the resulting glacial shapes were minor. The robustness of this model to the details of the sliding formulation reflects the partitioning of the total ice motion between sliding and deformation, both of which reduce the driving stress by transporting ice more rapidly through areas of locally high gravitational driving stress. Ice motion by these two processes always transports ice in the direction that lowers the local ice surface slope (hence gravitational driving stress); in our formulations of these processes, as in most formulations, the magnitude of this transport is greater where the gravitational driving stress is greater. If sliding is reduced, the resulting increase in ice thickness and ice surface slope increase the gravitational driving stress, which in turn increases deformation, and vise
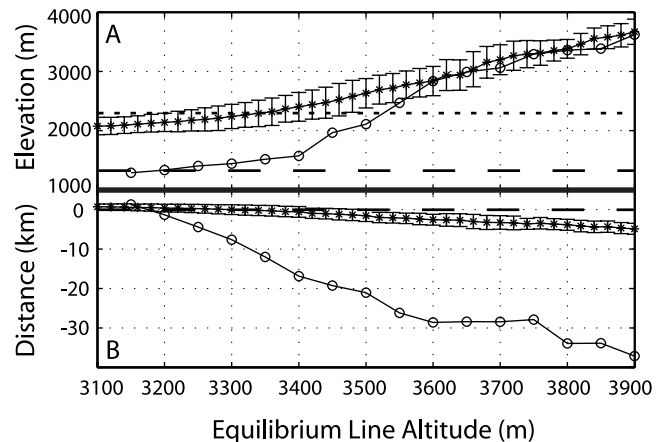

Figure 10. Termini elevations and relative positions in Experiments 1 and 2. (a) Kings Canyon terminus elevation (circles) and mean of eastern flank termini elevations (asterisks) as a function of imposed equilibrium line altitude. Kings Canyon LGM terminus elevation at ~1300 m (dashed line); mean of observed eastern flank termini elevations at ~2300 m (dotted line). (b) Mean straight line distance from the observed termini to the simulated termini positions on the eastern flank (asterisks) and in Kings Canyon on the western flank (circles) [*Moore*, 2000]. Positive and negative distances indicate simulated termini that have respectively overshot or not reached their LGM moraines. Dashed line indicates zero mean distance.
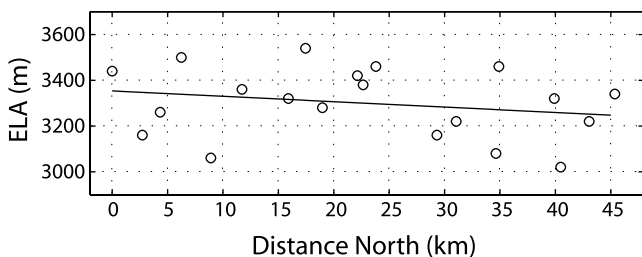
Figure 11. Predicted LGM ELAs for glaciers on the eastern flank of the Sierra Nevada range east of Kings Canyon. The ELA at the latitude of Kings Canyon is 3290 ± 60 m, with a north-to-south ELA gradient of 2.4 ± 2.4 m/km.

versa. The simulated glacial extent is therefore largely immune to the details of the ice transport algorithms.

[36] The sensitivities of the predicted LGM ELA to the imposed mass balance gradient, ∇b_z, and the maximum mass balance, b_z^{max}, were also explored; factor of two changes in either of these parameters resulted in ~100- to ~200-m changes in the predicted ELA. Increasing b_z^{max} raises the ELA necessary for the simulated glacier to reach the observed LGM terminus position by increasing the total accumulation. Increasing ∇b_z lowers the predicted LGM ELA. This reflects the capping of mass balance at high elevations, making the increase in total ablation greater than the increase in total accumulation; the predicted ELA must therefore drop to bolster the accumulation. That the simulated glacier extents show only modest sensitivity to these climate parameters indicates that the predictions of ELA are fairly robust; however, because some sensitivity exists this technique could be useful for determining values for these other climate parameters if the ELA can otherwise be constrained. As noted by *Plummer and Phillips* [2003], different climate scenarios that produce the same glacial extents in a single valley can be distinguished by considering the glacial extents in multiple valleys because individual valleys respond differently to a single climate forcing; therefore, all three climate parameters could possibly be constrained by simultaneously finding the best-fitting glacial extents within several valleys.

3.2. Experiment 2: Eastern Flank Equilibrium Line Altitude Lowering

[37] We now seek an explanation for the remaining asymmetry in glacial lengths, i.e., the roughly 1-km overshoot of simulated eastern glacier termini. We hypothesize that the overshoot in Experiment 1 can be explained by a higher average ELA on the eastern flank. We performed the ELA-lowering procedure shown in the first experiment on the eastern flank to determine how much higher the ELA would need to be on the eastern flank to account for the shorter observed LGM glaciers as compared with those simulated in Experiment 1. We ran this simulation only on the eastern half of the domain in Figure 1. Because the average intrinsic timescale for modeled eastern flank glaciers (~25 years) is about half that of the South Fork Kings Canyon glacier (~50 years), we reduced the time between ELA-lowering events to 200 years. To improve resolution of the estimated ELA, we reduced the ELA step size to 20 m, but made no attempt to reduce the step size further as the termini approached their LGM positions.

[38] The best-fitting ELA for each glacier on the eastern flank is plotted in Figure 11 as a function of distance north of the southernmost glacier terminus. The predicted ELA at the latitude of Kings Canyon is 3290 ± 60 m, the range deriving from the variability between independent glaciers on the eastern flank. The east-west asymmetry in glacier length that cannot be accounted for by topography can be accounted for by an east side mean ELA that is 120 m higher than the western flank value of 3170 m.

[39] Assuming an accumulation area ratio (AAR) of 0.65, the eastern flank LGM ELA at the latitude of Kings Canyon, inferred from moraine evidence, is 3110 ± 20 m [*Gillespie*, 1991]. While assuming an AAR of 0.65 is standard for determining paleo-ELAs [e.g., *Meierding*, 1982; *Porter*, 1975; *Gillespie*, 1991; *Burbank*, 1991], it neglects the substantial variation in AAR observed in extent glaciers, which for alpine glaciers is typically between 0.5 and 0.8 [*Meier and Post*, 1962]. The mean AAR for simulated LGM glaciers on the eastern flank is 0.61 ± 0.05, close to the typically assumed value of 0.65, but it ranges from 0.47 to 0.69. In this simulation, the wide range of AAR values is due entirely to local topography, as climate, through the mass balance function, is specified to be uniform. For a glacier at steady state, the average accumulation rate times the area of the accumulation zone must equal the average ablation rate times the area of the ablation zone. For a given mass balance profile, the detailed distribution of elevations in a particular valley influences the AAR at steady state by enforcing this balance [e.g., *Anderson et al.*, 2006].

3.3. Experiment 3: Orographic Precipitation—Positive Degree-Day Melt

[40] In the Experiments 1 and 2 we assumed a very simple mass balance function that required three high level parameters (*ELA*, ∇b_z, and b_z^{max}) that are black boxes encapsulating effects of temperature, precipitation and other more fundamental climate variables. In a third numerical experiment, we break open those black boxes by explicitly calculating the positive (accumulation) and negative (ablation) components of the mass balance field using the orographic precipitation and positive degree-day melt algorithms described in section 2.2.2. The objective of this experiment was to determine if the ~1-km overshoot of the observed eastern glacial extents in Experiment 1 and the east-west differences in ELA deduced from experiment 2 could be explained by a physically realizable orographic precipitation shadow.

[41] We first calibrated the orographic model by fitting the parameters C_α (scales topographically derived precipitation) and Δx (scales downwind advection) in an attempt to produce the modern pattern of precipitation across the Sierra Nevada (Figures 6 and 12) (WRCC, http://www.wrcc.dri.edu/summary/climsmsca.html) (fitted values: $C_\alpha = 5.9$, $\Delta x = 3.5$ km). On the upwind, western, side of the range the simulated precipitation agrees substantially with the modern recorded precipitation. On the downwind, eastern, side the gross characteristics of the precipitation shadow are simulated quite well; however, the simulated shadow predicts an even lower precipitation than that observed, which may indicate that the modern precipitation on the eastern flank is not entirely orographically derived (e.g., summer monsoon precipitation).
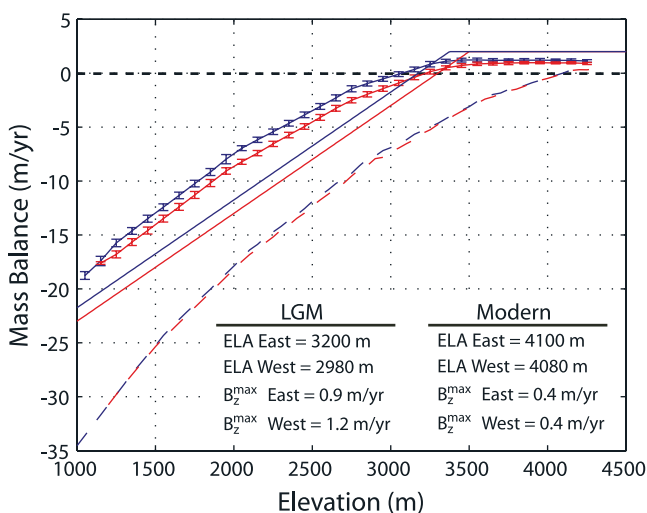
Figure 12. Average net mass balance versus elevation for modern and LGM (−5.6°C, 1.9 times the modern number of storms) climate parameters (dashed and solid colored lines, respectively). Straight line indicates the east and west mass balance as determined from Experiments 1 and 2. Curves are derived from the orographic precipitation and positive degree day melt models used in Experiment 3. Red and blue lines indicate mass balance on the eastern and western flanks respectively. The 1 standard deviation error bars indicate the range of mass balances in the model at that elevation. At high elevations, the eastern and western average balance curves level off at 0.9 m/yr and 1.2 m/yr, respectively. Horizontal dotted line indicates zero net mass balance.

[42] In this experiment, we ran a suite of simulations in which different combinations of temperature and precipitation anomalies were imposed and glaciers were permitted to reach their steady state sizes; other variables such as wind velocity were not explored. Temperature anomalies were expressed as absolute temperature changes from the modern temperature; precipitation anomalies were prescribed as a multiple of the modern number of storms per year. We note that increasing the number of storms linearly increases the total precipitation and roughly linearly increases the solid phase precipitation; however, it does not proportionately increase the net mass balance (precipitation minus melt) because it does not affect the melt rate.

[43] We report the precipitation/temperature pairings that produced glacier termini positions in Kings Canyon that best match the observed LGM position (Figure 13a). All of the temperature/precipitation pairs along the curve in Figure 13a reproduce the observed 37.8 km long glacier in Kings Canyon. With no change in precipitation, a lowering of temperature by 7.8°C is required to reproduce the LGM glacial extents in Kings Canyon; with no change in temperature, ∼11 times the modern number of storms is required. When assuming no increase in precipitation, *Plummer and Phillips* [2003] estimated an LGM temperature depression of 6.5°C using a similar 2-D modeling technique in Bishop Creek on the eastern flank. The shifted squared relationship indicates that the effect of temperature lowering is greater than that of increasing precipitation. This may result from the multiplicative effect of temperature
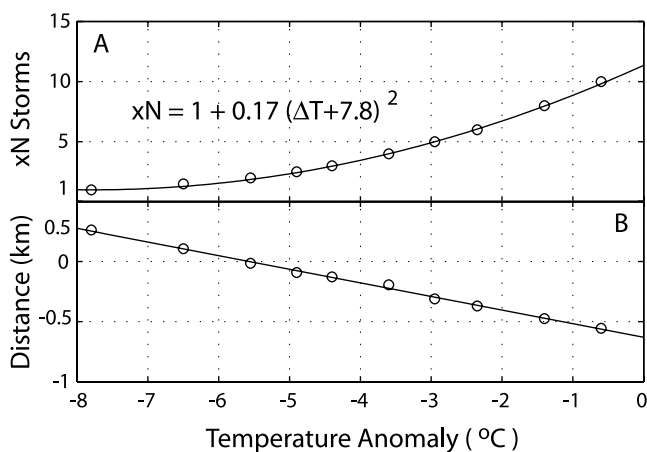

Figure 13. (a) Multiple of the modern number of storms versus temperature anomaly (ΔT) from the modern temperature. The curve indicates a shifted square fit through the *x-y* pairs (circles) that produce glacial extents in Kings Canyon matching observed LGM extents [*Moore*, 2000]. (b) Mean distance from the simulated termini to the observed LMG termini on the eastern flank, with positive and negative distances indicting simulated termini that respectively overshoot or undershoot their observed LGM positions.

decrease on the mass balance: first, a greater fraction of the precipitation falls in the solid phase (Figure 14), and second, the melt rates decrease in the accumulation and ablation zones.

[44] A simulation with 11.3 times the number of storms produced a net mass balance in the accumulation zone that was 3–4 times the mass balance with no precipitation anomaly and a 7.8°C temperature depression. Although these two scenarios produce a similar glacier footprint in Kings Canyon, the high storm frequency glacier is ∼30% thicker on average, slides on average ∼50% faster, and has on average 150% greater internal deformation. However, these average differences are dominated by large regions of thin ice; for example, the centerline thickness in the main canyon differs by less than 3%. These large increases in velocity are reasonable since internal deformation goes as the fourth power of ice thickness. The expected threefold to fourfold increase in ice discharge from the accumulation
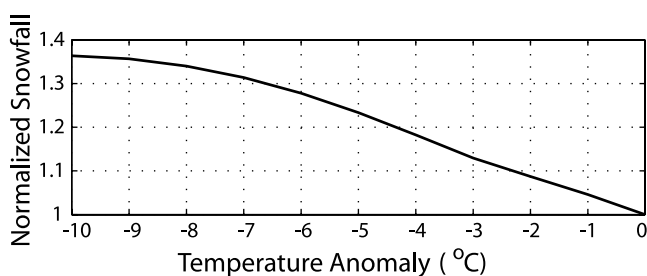

Figure 14. Solid phase precipitation in Kings Canyon as a function of temperature anomaly normalized by the precipitation at zero temperature depression (modern temperature). Decreasing the temperature increases the total precipitation that falls in the solid phase.

zone to the ablation zone results from a ~75% greater total ice velocity, a ~30% greater ice thickness, and a ~35% greater glacier width at the ELA, which is 200 m lower in the no-precipitation anomaly scenario. This additional ice transfer is required at steady state in order to balance the higher mass balance gradient (also known as the activity index [*Meier*, 1961]) that this climate scenario produces. These end-member climate scenarios therefore result in glaciers that are significantly different in character despite their similar footprint. We note that the higher precipitation rate glacier would presumably erode the landscape more quickly, as erosion is intimately tied to sliding rates.

[45] While the moraine position in Kings Canyon alone does not constrain the LGM temperature/precipitation anomaly pair, the many glaciers on the eastern flank allow us to disentangle which pair is most appropriate for the LGM climate. We seek the anomaly pair that minimizes the mean distance between the simulated and the observed eastern flank termini (Figure 13b). The distance between a simulated terminus and an observed terminus was considered positive if the simulated glacier overshot the observed LGM terminus. The climate scenario that best fits the LGM termini positions of east-flank glaciers is one in which precipitation is 1.9 times the modern rate and temperature is depressed by 5.6°C (Figure 13b).

[46] Our paleoclimate results can be compared to Experiments 1 and 2, as well as earlier studies, by determining the ELA from the mass balance field (Figure 12). The best-fitting climate scenario results in an LGM ELA on the western flank of 2980 m, while on the eastern flank it is 3200 m. This western flank value is ~200 m lower than the ELA that produced the best-fitting Kings Canyon glacier in Experiment 1 (3170 m), and reflects a lower average mass balance in the accumulation zone. In Experiment 1, the net mass balance above ~3400 m was set by the 2 m/yr imposed maximum mass balance, b_z^{max}, while in this experiment the mean net mass balance above ~3400 m is only ~1.2 m/yr. The average accumulation zone mass balances in Kings Canyon differ by about the same factor: 0.8 m/yr and 0.5 m/yr for Experiments 1 and 3, respectively. The lower accumulation zone mass balance of Experiment 3 demands a lower ELA to achieve the same steady state glacier extents. The ~90 m discrepancy between ELA estimates for eastern flank glaciers in Experiments 2 (ELA = 3290 m) and 3 (ELA = 3200 m) is smaller in part because the higher eastern flank ELA results in less of the total accumulation area (only elevations above ~3500 m) being limited by the maximum mass balance, b_z^{max}, which is the primary cause of the change in predicted ELA on the western flank.

3.4. Experiment 4: North-South Temperature Gradient

[47] The orographic and positive degree-day algorithms used in Experiment 3, which explicitly include temperature through the saturation vapor pressure, the phase of the precipitation, and the magnitude of the annual melt, can be used to assess spatial variation in temperature. In a final numerical experiment, we ran a series of simulations in which a range of north-south gradients in temperature were imposed; in each simulation the mean annual temperature declined from south to north with a prescribed gradient. The objective of this experiment was to determine the north-

south temperature gradient that best matched the glacier extents on the eastern flank. We used the mean of the distances between the simulated termini and the observed termini as a measure of how well the temperature gradient matched the actual gradient. The best fitting temperature gradient is 3.5 ± 2.5°C/°latitude north-to-south.

[48] For comparison with both observations and Experiment 2, the ELA gradient from north-to-south on the eastern flank in this experiment was determined from the mass balance pattern in the best fitting simulation. The resulting north-to-south ELA gradient of 3.7 ± 0.3 m/km (this error range only reflects ELA variation within the best fitting simulation) is roughly consistent with a previous estimate of the early Tioga ELA gradient of 3.1 ± 0.2 m/km [*Gillespie*, 1991], which is based upon the AAR method. The AAR method has also been used to infer the north-to-south ELA gradient during the late Tioga glaciation of the Sierra Nevada (2.2 ± 1.0 m/km) [*Gillespie*, 1991] and the modern ELA gradient (2.0 m/km) [*Burbank*, 1991].

[49] In Experiment 2 we solved for the best-fitting ELA in each valley independently; the ELA gradient along the eastern flank found through linear regression is 2.4 ± 2.4 m/km (Figure 11). Although the predicted value is in agreement with estimates from AAR-based reconstructions [*Gillespie*, 1991; *Burbank*, 1991] and from Experiment 4, there is substantial uncertainty in our estimate of the north-south gradient in ELA. Experiments 2 and 4 both fail to tightly constrain the temperature gradient largely because of the short segment of range encompassed in this study (50 km versus ~400 km in other studies [*Gillespie*, 1991]); the systematic decrease in termini elevations owing to decline in temperature from south to north is small compared to the large misfit between simulated and observed termini owing to physics not included in this model or error in the observed termini positions.

4. Discussion and Conclusions

[50] The primary objectives of this study were to determine how much of the east-west difference in glacier length in the Sierra Nevada results from asymmetry in topography and how much results from asymmetry in climate, and more generally to further demonstrate the utility of 2-D numerical glacier simulations in reconstruction of paleoclimate. In the first numerical experiment, we determined that the asymmetry in topography accounts for 97% of the east-west difference in LGM glacier lengths. Even within the Sierra Nevada, which receives abundant orographic precipitation and casts one of the more pronounced rainshadows in the world, topographic asymmetry exerts the primary control on glacier lengths.

[51] Although the ELA is often used as a single proxy for past climate in glaciated areas, variations in ELA are ambiguous because a change in ELA could result from changes in any number of physical parameters (e.g., winter or summer temperature, wind speed, precipitation). In contrast, more fundamental climate parameters such as precipitation and temperature can be used to drive physically based glacial models with a more appropriate spatially variable climate. In Experiment 3 we show that a simple, orographically influenced pattern of precipitation can account for the ~1-km overshoot of the observed eastern flank

glacial extents in Experiment 1. Using the natural experiment of the east and west-draining valleys in the Sierras, in which tens of glaciers allow us to constrain spatial variability in climate, models run in Experiment 3 suggest that the pattern of LGM moraines can be best explained by a 5.6°C lowering of temperature and a doubling of the number of storms. In addition, while less well constrained given the latitudinal extent of the calculation space, models run in Experiment 4 suggest a 3.5°C/°latitude north-to-south temperature gradient during the LGM and a north-to-south ELA gradient of 3.7 m/km. However, over this short segment of the Sierra Nevada, the majority of the ELA variation likely results from the effect of topography on local precipitation and melt, while the latitudinal temperature gradient plays a minor role.

[52] Our result of 5.6°C cooling and twice the precipitation for LGM conditions is reasonable when compared with previous estimates of the LGM climate. Previous climate mass balance modeling suggests that Sierra Nevada glaciers were unique among western North American glaciers in that they required increased precipitation to reach LGM termini positions [*Hostetler and Clark*, 1997]. Climate models of western North America indicate that during the LGM the jet stream was deflected southward by polar high-pressure systems resulting from expansion of the Laurentide ice sheet and mountain glaciers [e.g., *Bartlein et al.*, 1998]. The southward deflection of the mean jet stream position resulted in more frequent winter storms that increased precipitation across much of western and southwestern North America [*Thompson et al.*, 1993; *Bartlein et al.*, 1998]. Additionally, lower LGM temperatures would have extended the accumulation season and shortened the ablation season [*Leonard*, 1989]. To the west of the Sierra Nevada, marine records suggest intervals of increased precipitation in the Coast Ranges during glacial and early interglacial periods [*Robert*, 2004]. East of the range, floral assemblages in packrat middens around Yucca Mountain, Nevada, indicate a mean LGM temperature depression of 7.5°C and at least a 2.4-fold increase in precipitation [*Thompson et al.*, 1999]. The presence of large lakes in the Great Basin region during glacial periods indicates a regionally cooler and wetter climate [e.g., *Smith and Street-Perrott*, 1983; *Benson and Thompson*, 1987; *Benson et al.*, 1990]. Water balance modeling indicates that lake level changes were driven more by variations in precipitation than in temperature [*Phillips et al.*, 1992]. Further east, former lake levels in the Estancia basin, New Mexico, suggest a mean LGM temperature depression of 5.0°C and a 2.0-fold increase in precipitation [*Menking et al.*, 2004]. That our results closely match these independent estimates of LGM temperature and precipitation increases our confidence in the model.

[53] We argue that the insensitivity of this model to the details of the ice motion physics is due to the nature of glaciers. First, two ice transport processes, sliding and internal deformation, act to reduce the gravitational driving stress, which is the force causing ice motion. Reduction of the role of one process by modification of its formulation or its parameters enhances the role of the other process by effectively raising the driving stress, ultimately leading to only a small modification in ice extent. Second, the extent of glaciation under a given climate and for a given topog-raphy is as much a result of strong feedbacks between the topography, the glacier that grows within it, and the climate as it is to the details of the ice physics. For example, as a glacier occupies more of its valley it raises the surface elevation at which the climate boundary condition is being applied, both reducing the melt rate and increasing the precipitation. This increases the accumulation area, causing the glacier to grow further. Even the simplest model that contains some reasonable prediction of ice thickness will capture the essence of this important feedback. However, other feedbacks, for example between hydrology and ice motion, or between ice surface height and radiation shadowing, are not as yet incorporated in our model. While further refinement is therefore needed, we argue that the glacier model in its present state is already a powerful tool for addressing paleoclimate questions in topographically complex terrain.

Appendix A

[54] A number of formulations have been used to model basal sliding, all of which compute the sliding velocity from the basal shear stress, τ_b. A typical formulation is [e.g., *Fastook and Chapman*, 1989; *Paterson*, 1994; *Plummer and Phillips*, 2003]

$$U_s = fB\tau_b^m, \tag{A1}$$

in which f is a fraction between 0 and 1 that partitions the ice motion between deformation and sliding, B is a constant, and the exponent m is generally taken to be 2 [*Paterson*, 1994].

[55] One formulation that acknowledges the role of glacial hydrology scales the sliding velocity inversely with the effective pressure (N = ice pressure − water pressure) at the bed [e.g., *Budd et al.*, 1979; *Bindschadler*, 1983; *Kessler and Anderson*, 2004],

$$U_s = B\tau_b^m N^{-p}. \tag{A2}$$

In this formulation sliding speed can go infinite when N = 0. While this may resemble fast sliding events, in nature the sliding velocity remains finite even when the water pressure exceeds the ice pressure, as longitudinal coupling to upstream and downstream ice inhibits sliding.

[56] Another formulation that incorporates the hydrology, but which may give more realistic behavior at high water pressure, scales the sliding velocity by the flotation fraction (water pressure over ice pressure) [*Marshall et al.*, 2005],

$$U_s = B\frac{P_w}{P_i}\tau_b. \tag{A3}$$

Here the sliding velocity is linearly proportional to the basal shear stress ($m = 1$ in equations (A1) and (A2)). The sliding speed scales linearly with the water pressure. Given our limited knowledge of the sliding process in many cases this simple and elegant formulation is an appealing alternative.

[57] A sliding law that incorporates glacial hydrology may be appropriate for investigating the short term variations in sliding velocity; however, its inclusion in a longer timescale model, such as presented here, is difficult to

justify given that the water table is not a simple function of slowly changing geometrical parameters (i.e., ice thickness), but instead entails complex interactions between the glacier and its seasonally variable hydrologic system (see for example simulations from *Kessler and Anderson* [2004], and the formulations of *Flowers and Clarke* [2002a, 2002b]). In addition, if sliding varies nonlinearly with the effective pressure then a simple time average of the water pressure is insufficient.

References

Alpert, P. (1986), Mesoscale indexing of the distribution of orographic precipitation over high mountains, *J. Clim. Appl. Meteorol.*, 25, 532–545.

Anders, A. M., G. H. Roe, and D. R. Duran (2004), Orographic precipitation and the form of mountain ranges, *Bull. Am. Meteorol. Soc.*, 85(4), 498–499.

Anderson, R. S., S. P. Anderson, K. R. MacGregor, S. O'Neel, C. A. Riihimaki, E. D. Waddington, and M. G. Loso (2004), Strong feedbacks between hydrology and sliding of a small alpine glacier, *J. Geophys. Res.*, 109, F03005, doi:10.1029/2004JF000120.

Anderson, R. S., P. Molnar, and M. A. Kessler (2006), Features of glacial valley profiles simply explained, *J. Geophys. Res.*, 111, F01004, doi:10.1029/2005JF000344.

Bak, P., C. Tang, and K. Wiesenfeld (1988), Self-organized criticality, *Phys. Rev. A*, 38, 364–374.

Bartlein, P. J., K. H. Anderson, P. M. Anderson, M. E. Edwards, C. J. Mock, R. S. Thompson, R. S. Webb III, and C. Whitlock (1998), Paleoclimate simulations for North America over the past 21,000 years: Features of the simulated climate and comparisons with paleoenvironmental data, *Quat. Sci. Rev.*, 17, 549–585.

Bateman, P. C., and C. Wahrhaftig (1966), Geology of the Sierra Nevada, in *Geology of Northern California*, edited by E. H. Bailey, *Bull. Calif. Div. Mines Geol.*, 190, 107–172.

Benson, L., and R. S. Thompson (1987), The physical record of lakes in the Great Basin, in *North America and Adjacent Oceans During the Last Deglaciation*, *Geol. N. Am.*, vol. K-3, edited by W. F. Ruddiman and H. E. Wright Jr., pp. 241–260, Geol. Soc. of Am., Boulder, Colo.

Benson, L. V., D. R. Currey, R. I. Dorn, K. R. Lajoie, C. G. Oviatt, S. W. Robinson, G. I. Smith, and S. Stine (1990), Chronology of expansion and contraction of four Great Basin lake systems during the past 35,000 years, *Palaeogeogr. Palaeoclimatol. Palaeoecol.*, 78, 241–286.

Bindschadler, R. (1983), The importance of pressurized subglacial water in separation and sliding at the glacier bed, *J. Glaciol.*, 29(101), 3–19.

Birman, J. H. (1964), Glacial geology across the crest of the Sierra Nevada, *Spec. Pap. Geol. Soc. Am.*, 75, 80 pp.

Blackwelder, E. (1931), Pleistocene glaciation of the Sierra Nevada and Basin Ranges, *Geol. Soc. Am. Bull.*, 42, 865–922.

Braithwaite, R. J. (1995), Positive degree-day factors for ablation on the Greenland ice sheet studied by energy-balance modeling, *J. Glaciol.*, 41(137), 153–160.

Budd, W. F., P. L. Keage, and N. A. Blundy (1979), Empirical studies of ice sliding, *J. Glaciol.*, 23(89), 157–170.

Burbank, D. W. (1991), Late Quaternary snowline reconstructions for the southern and central Sierra Nevada, California and a reassessment of the "Recess Peak Glaciation," *Quat. Res.*, 36, 294–306.

Clark, D. H., A. R. Gillespie, M. Clark, and R. Burke (2003), Mountain glaciations of the Sierra Nevada, in *Quaternary Geology of the United States: INQUA 2003 Field Guide Volume*, edited by D. J. Easterbrook, pp. 287–311, Desert Res. Inst., Reno, Nev.

Fastook, J., and J. E. Chapman (1989), A map-plane finite element model: Three modeling experiments, *J. Glaciol.*, 35(119), 48–52.

Flowers, G. E., and K. C. Clarke (2002a), A multicomponent coupled model of glacier hydrology: 1. Theory and synthetic examples, *J. Geophys. Res.*, 107(B11), 2287, doi:10.1029/2001JB001122.

Flowers, G. E., and K. C. Clarke (2002b), A multicomponent coupled model of glacier hydrology: 2. Application to Trapridge Glacier, Yukon, Canada, *J. Geophys. Res.*, 107(B11), 2288, doi:10.1029/2001JB001124.

Gillespie, A. R. (1991), Testing a new climatic interpretation for the Tahoe glaciation, in *Natural History of Eastern California and High-Altitude Research: White Mountain Research Station Symposium Volume*, edited by C. A. Hall, V. Doyle-Jones, and B. Widawski, pp. 383–398, Univ. of Calif., Los Angeles, Los Angeles.

Harper, J. T., and N. F. Humphrey (2003), High-altitude Himalayan climate inferred from glacial ice flux, *Geophys. Res. Lett.*, 30(14), 1764, doi:10.1029/2003GL017329.

Hooke, R. L. (2005), *Principles of Glacier Mechanics*, 2nd ed., 429 pp., Cambridge Univ. Press, New York.

Hostetler, S. W., and P. U. Clark (1997), Climatic controls of western U.S. glaciers at the Last Glacial Maximum, *Quat. Sci. Rev.*, 16, 505–511.

Iken, A., and R. A. Bindschadler (1986), Combined measurements of subglacial water pressure and surface velocity of Findelengletscher, Switzerland: Conclusions about drainage system and sliding mechanism, *J. Glaciol.*, 32(110), 101–119.

Kessler, M. A., and R. S. Anderson (2004), Testing a numerical glacial hydrological model using spring speed-up events and outburst floods, *Geophys. Res. Lett.*, 31, L18503, doi:10.1029/2004GL020622.

Leonard, E. M. (1989), Climatic change in the Colorado Rocky Mountains: Estimates based on modern climate at Late Pleistocene equilibrium lines, *Arct. Alp. Res.*, 21(3), 245–255.

MacGregor, K. R., R. S. Anderson, S. P. Anderson, and E. D. Waddington (2000), Numerical simulations of glacial-valley longitudinal profile evolution, *Geology*, 28, 1031–1034.

Marshall, S. J., H. Björnsson, G. E. Flowers, and G. K. C. Clarke (2005), Simulation of Vatnajökull ice cap dynamics, *J. Geophys. Res.*, 110, F03009, doi:10.1029/2004JF000262.

Mayo, L. R. (1984), Glacier mass balance and runoff research in the U. S. A., *Geogr. Ann., Ser. A, Phys. Geogr.*, 66(3), 215–227.

Meier, M. F. (1961), Mass budget of South Cascade Glacier, 1957–60, *U.S. Geol. Surv. Prof. Pap.*, 242-B, 206–211.

Meier, M. F., and A. Post (1962), Recent variations in mass net budgets of glaciers in western North America, *Int. Assoc. Hydrol. Sci.*, 58, 63–77.

Meier, M. F., W. V. Tangborn, L. R. Mayo, and A. Post (1971), Combined ice and water balances of Gulkana and Wolverine glaciers, Alaska, and South Cascade glacier, Washington, 1965 and 1966 hydrologic years, *U.S. Geol. Surv. Prof. Pap., 715-A*, 23 pp.

Meierding, T. C. (1982), Late Pleistocene glacial equilibrium-line altitudes in the Colorado Front Range: A comparison of methods, *Quat. Res.*, 18, 289–310.

Menking, K. M., R. Y. Anderson, N. G. Shafike, K. H. Syed, and B. D. Allen (2004), Wetter or colder during the Last Glacial Maximum? Revisiting the pluvial lake question in southwestern North America, *Quat. Res.*, 62, 280–288.

Moore, J. G. (2000), *Exploring the Highest Sierra*, 427 pp., Stanford Univ. Press, Stanford, Calif.

Oerlemans, J. (1986), An attempt to simulate historic front variations of Nigardsbreen, Norway, *Theor. Appl. Climatol.*, 37(3), 126–135.

Pandey, G. R., D. R. Cayan, and K. P. Georgakakos (1999), Precipitation structure in the Sierra Nevada of California, *J. Geophys. Res.*, 104(D10), 12,019–12,030.

Paterson, W. S. B. (1994), *The Physics of Glaciers*, 3rd ed., 481 pp., Elsevier, New York.

Phillips, F. M., A. R. Campbell, C. Kruger, P. Johnson, R. Roberts, and E. Keyes (1992), *A Reconstruction of the Response of the Water Balance in Western United States Lake Basins to Climate Change*, vol. 1, *Rep. 269*, 167 pp., Water Resour. Res. Inst., Las Cruces, N. M.

Plummer, M. A., and F. M. Phillips (2003), A 2-D numerical model of snow/ice energy balance and ice flow for paleoclimatic interpretation of glacial geomorphic features, *Quat. Sci. Rev.*, 22, 1389–1406.

Porter, S. C. (1975), Equilibrium-line altitudes of Late Quaternary glaciers in the Southern Alps, New Zealand, *Quat. Res.*, 5, 27–47.

Robert, C. (2004), Late Quaternary variability of precipitation in Southern California and climatic implications: Clay mineral evidence from the Santa Barbara Basin, ODP Site 893, *Quat. Sci. Rev.*, 23, 1029–1040.

Roe, G. H. (2005), Orographic precipitation, Annu. Rev, *Earth Planet. Sci.*, 33, 645–671.

Roe, G. H., D. R. Montgomery, and B. Hallet (2002), Effects of orographic precipitation variations on the concavity of steady-state river profiles, *Geology*, 30, 143–146.

Smith, G. I., and F. A. Street-Perrott (1983), Pluvial lakes of the western United States, in *Late-Quaternary Environments of the United States*, vol. 1, *The Late Pleistocene*, edited by S. C. Porter, pp. 190–214, Univ. of Minn. Press, Minneapolis.

Smith, J. A., G. O. Seltzer, D. L. Farber, D. T. Rodbell, and R. C. Finkel (2005), Early local Last Glacial Maximum in the tropical Andes, *Science*, 308, 678–681.

Thompson, R. S., C. Whitlock, P. J. Bartlein, S. P. Harrison, and W. G. Spaulding (1993), Climatic changes in the western United States since

18,000 yr B. P., in *Global Climates Since the Last Glacial Maximum*, edited by H. E. Wright Jr. et al., pp. 465–513, Univ. of Minn. Press, Minneapolis.

Thompson, R. S., K. H. Anderson, and P. J. Bartlein (1999), Quantitative paleoclimatic reconstructions from late Pleistocene plant macrofossils of the Yucca Mountain region, *U.S. Geol. Surv. Open File Rep.*, 99-338, 39 pp.

Wahrhaftig, C., and J. H. Birman (1965), The Quaternary of the Pacific mountain system in California, in *The Quaternary of the United States*, edited by H. E. Wright Jr. and D. G. Frey, pp. 299–340, Princeton Univ. Press, Princeton, N. J.

Werner, B. T. (1995), Eolian dunes: Computer simulations and the attractor interpretation, *Geology*, *23*, 1107–1110.

―――――――――――――

R. S. Anderson, Department of Geological Sciences and Institute for Arctic and Alpine Research, University of Colorado, Boulder, CO 80309, USA.

M. A. Kessler, Institute for Arctic and Alpine Research, University of Colorado, Boulder, CO 80309, USA. (mark.kessler@colorado.edu)

G. M. Stock, Department of Geological Sciences, University of Michigan, Ann Arbor, MI 48109-1005, USA.